FSHD2- and BAMS-associated mutations confer opposing effects on SMCHD1 function

Received for publication, March 23, 2018, and in revised form, May 3, 2018 Published, Papers in Press, May 10, 2018, DOI 10.1074/jbc.RA118.003104

Alexandra D. Gurzau[‡§1], Kelan Chen[‡§1], Shifeng Xue[¶‖], Weiwen Dai[‡], Isabelle S. Lucet[‡§], Thanh Thao Nguyen Ly[¶‖], Bruno Reversade[¶‖‡‡§§], Marnie E. Blewitt[‡§¶¶2], and James M. Murphy[‡§3]**

*From the [‡]Walter and Eliza Hall Institute of Medical Research, 1G Royal Parade, Parkville, Victoria 3052, Australia, the Departments of [§]Medical Biology and [¶¶]Genetics, University of Melbourne, Parkville, Victoria 3052, Australia, the [¶]Institute of Molecular and Cell Biology and [‖]Human Genetics and Embryology Laboratory, Institute of Medical Biology, A*STAR, Singapore, the **Department of Medical Genetics, Koç University School of Medicine (KUSoM), 34450 Sarıyer/Istanbul, Turkey, the [‡‡]Department of Paediatrics, School of Medicine, National University of Singapore, Singapore, and [§§]Amsterdam Reproduction and Development, Academic Medical Centre and VU University Medical Center, 1105 AZ Amsterdam, The Netherlands*

Edited by Eric R. Fearon

Structural maintenance of chromosomes flexible hinge domain-containing 1 (Smchd1) plays important roles in epigenetic silencing and normal mammalian development. Recently, heterozygous mutations in *SMCHD1* have been reported in two disparate disorders: facioscapulohumeral muscular dystrophy type 2 (FSHD2) and Bosma arhinia microphthalmia syndrome (BAMS). FSHD2-associated mutations lead to loss of function; however, whether BAMS is associated with loss- or gain-of-function mutations in SMCHD1 is unclear. Here, we have assessed the effect of *SMCHD1* missense mutations from FSHD2 and BAMS patients on ATP hydrolysis activity and protein conformation and the effect of BAMS mutations on craniofacial development in a *Xenopus* model. These data demonstrated that FSHD2 mutations only result in decreased ATP hydrolysis, whereas many BAMS mutations can result in elevated ATPase activity and decreased eye size in *Xenopus*. Interestingly, a mutation reported in both an FSHD2 patient and a BAMS patient results in increased ATPase activity and a smaller *Xenopus* eye size. Mutations in the extended ATPase domain increased catalytic activity, suggesting critical regulatory intramolecular interactions and the possibility of targeting this region therapeutically to boost SMCHD1's activity to counter FSHD.

This study was supported by an Australian Research Training Program scholarship (to A. D. G.), a Cancer Council Victoria fellowship (to K. C.), the Bellberry-Viertel Senior Medical Research Fellowship (to M. E. B.), Australian National Health and Medical Research Council Fellowship 1105754 (to J. M. M.) and Grant 1098290 (to M. E. B. and J. M. M.), A*STAR BMRC YIG (to S. X.), NMRC YIRG (to S. X.), and a Strategic Positioning Fund on Genetic Orphan Diseases from the BMRC, A*STAR, Singapore (to B. R.). Additional support was provided by Victorian State Government Operational Infrastructure Support, Australian National Health and Medical Research Council IRIISS Grant 9000433, and the Australian Cancer Research Foundation. The authors declare that they have no conflicts of interest with the contents of this article.

This article contains Tables S1 and S2 and Figs. S1 and S2.

[1] Both authors contributed equally to this work.

[2] To whom correspondence may be addressed: Walter and Eliza Hall Institute of Medical Research, 1G Royal Parade, Parkville, Victoria 3052, Australia. Tel.: 61-3-93452555; E-mail: blewitt@wehi.edu.au.

[3] To whom correspondence may be addressed: Walter and Eliza Hall Institute of Medical Research, 1G Royal Parade, Parkville, Victoria 3052, Australia. Tel.: 61-3-93452555; E-mail: jamesm@wehi.edu.au.

SMCHD1 is a large chromosomal protein that has an established role in epigenetic silencing (1–3). Mutations in one copy of *SMCHD1* have recently been reported in two distinct diseases, facioscapulohumeral muscular dystrophy type 2 (FSHD2)[4] (4, 5) and Bosma arhinia microphthalmia syndrome (BAMS) (6, 7). The debate surrounding the effect of the BAMS mutations on SMCHD1 function plus the potential therapeutic benefit of targeting SMCHD1 in FSHD have made further study of these mutations of particular interest.

Smchd1 is considered a noncanonical member of the structural maintenance of chromosomes (SMC) protein family (2). Canonical SMC proteins have been shown to form various protein complexes within a cell and play a crucial role in chromosome architecture (8–10), presumably by entrapping and actively translocating across chromosomal DNA (11–13). Each SMC protomer consists of an ABC-type ATPase "head" and a DNA-binding, dimerization SMC hinge domain, linked via a long intramolecular coiled-coil region (14, 15). Recent studies on prokaryotic SMC proteins suggested that ATP hydrolysis drives a conformational transition between rod and ring-shaped structures of SMC dimers, with the central chamber formed in the latter conformation predicted to accommodate a DNA double helix (16). Smchd1 is considered a member of the SMC family owing to the presence of an SMC hinge domain. We recently demonstrated via small-angle X-ray scattering (SAXS), binding studies, and analytical ultracentrifugation that Smchd1's hinge domain likewise forms a homodimer (17). We also revealed that it retains a binding ability of both DNA and RNA *in vitro* (18), highlighting the possibility that it might interact with chromatin via an alternative method to canonical SMC proteins.

Unlike other members of the SMC family, Smchd1 has a putative ATPase domain at its N terminus that resembles a GHKL (gyrase, Hsp90, histidine kinase, MutL) ATPase (19, 20) rather than an ABC type present in other family members

[4] The abbreviations used are: FSHD1 and -2, facioscapulohumeral muscular dystrophy type 1 and 2, respectively; BAMS, Bosma arhinia microphthalmia syndrome; SMC, structural maintenance of chromosomes; SAXS, small-angle X-ray scattering; SEC, size-exclusion chromatography; TCEP, tris(2-carboxyethyl)phosphine; TSA, thermal stability assay; mP, millipolarization units; PDB, Protein Data Bank.

(Fig. 1*a*). Remarkably, we recently found that Smchd1's extended GHKL domain adopts a conformation that grossly resembles the full-length Hsp90 (heat-shock protein 90) molecular chaperone protein, and we and others have shown that Smchd1 is additionally antagonized by an Hsp90 inhibitor, radicicol (20, 21). These studies suggest that Smchd1 and Hsp90 proteins share a similar catalytic binding pocket. We have shown that this region of Smchd1 is catalytically active in its monomeric form, exhibiting an ATP turnover rate comparable with that of Hsp90 (20). This raises the possibility that Smchd1 may participate in structural manipulation of chromatin in an ATP-dependent manner as part of its role in gene expression regulation.

Heterozygous loss-of-function mutations in *SMCHD1* contribute to ~80% of FSHD2 cases (4). The autosomal dominant muscular condition, FSHD, is characterized by facial, shoulder, and upper arm muscle weakness and encompasses two disease types: FSHD type 1 (FSHD1), the more common form, and type 2 (FSHD2) (22). In both cases, the condition arises due to derepression of a macrorepeat array, *D4Z4*, located in the subtelomeric region of chromosome 4q, ultimately resulting in a more permissive local chromatin structure (23). In the presence of a polymorphic polyadenylation signal on the last *D4Z4* repeat, a stabilized *DUX4* mRNA arises, encoding a transcription factor that activates ectopic signaling pathways leading to skeletal muscle cell death and the phenotypic changes and symptoms common to patients suffering from either FSHD1 or FSHD2 (24, 25). In healthy humans, SMCHD1 directly binds to and maintains CpG methylation and a repressed chromatin structure at *D4Z4* repeats (4, 26, 27). In FSHD2 patients, reduced functional SMCHD1 levels result in derepression of the local chromatin structure at the *D4Z4* repeat array, allowing *DUX4* mRNA expression (26). Whereas FSHD1 is caused by contraction of the *D4Z4* repeat array, *SMCHD1* mutations in FSHD1 patients have been found to correlate with augmented disease severity (5, 28). These findings demonstrate that mutations in *SMCHD1* are not exclusively present in FSHD2 patients, as they can also act as a disease modifier in FSHD1 patients.

Adding to the complexity of pathogenesis arising from alterations in *SMCHD1*, mutations were recently associated with a rare congenital disorder, BAMS (6, 7). The condition is characterized primarily by a striking absence of the nasal area, often also accompanied by a reduction in eye size (29). Whole-exome sequencing of over 50 patients revealed *de novo* heterozygous missense mutations in *SMCHD1*, all of which mapped to the N-terminal GHKL-type ATPase domain and its adjacent extension domain, suggesting an altered enzymatic function in patients (6, 7). Using both *in vitro* and *in vivo* systems, we proposed that *SMCHD1* mutations affecting BAMS patients display a gain-of-function phenotype (6), as opposed to FSHD2 patients, who have been shown to harbor loss-of-function mutations that contrastingly occur throughout the *SMCHD1* gene (4). A parallel study carried out by Shaw *et al.* (7) also identified missense *SMCHD1* mutations in BAMS patients, which were proposed to underlie a loss of SMCHD1 function. However, the group did not use biochemical studies to investigate the catalytic function of their identified mutations, and their mouse models failed to recapitulate the BAMS phenotype. It is therefore of outstanding interest to define whether mutations in BAMS patients augment or suppress SMCHD1 activity.

Here, we report the biochemical properties of SMCHD1 variants, using the N-terminal GHKL ATPase– containing fragment. Analysis of all recombinant proteins via SAXS indicates similar structural features at low resolution, suggesting that a topology comparable with that of the WT counterpart is conserved among the mutants. We show that FSHD2-associated mutations in *SMCHD1* generally perturb the ATP hydrolysis ability of the recombinant proteins. In contrast, we observed enhanced ATPase activity in some BAMS-associated mutants and a decreased eye size in a *Xenopus* model of craniofacial development. These data are most consistent with the idea that BAMS arises from gain-of-function mutations in SMCHD1.

Results

Expression, purification, and thermal stability analyses of recombinant Smchd1 variants

To test the effect of BAMS- and FSHD-associated variants, we used our established baculovirus-insect cell platform to produce recombinant proteins encompassing the extended Smchd1 GHKL-ATPase domain (residues 111–702) (Fig. 1*a*) (20). Whereas WT Smchd1(111–702) gives rise to stable, catalytically active recombinant protein, we sought to establish the impact of substituting highly conserved residues corresponding to BAMS- and FSHD-associated variants (Fig. 1, *b–d*). All recombinant proteins were subjected to three rounds of protein purification: immobilized metal affinity chromatography, ion-exchange chromatography, and size-exclusion chromatography (SEC), where SEC elution profiles of all mutants resembled that of the monomeric WT protein (Fig. 2, *a–c*). The mutants were additionally subjected to a thermal denaturation assay to assess the impact of the mutations on protein stability (Fig. 2, *d–f*). Results indicate that the majority retain a WT-like thermal stability, with two BAMS-associated mutants, W342S and H348R, exhibiting the most significant reduction by ~4.3 and ~5.3 °C, respectively, as compared with WT protein.

Ab initio modeling from SAXS data reveals a conserved overall protein structure across the studied mutants

We examined the behavior of a large cohort of Smchd1(111–702) mutants using SAXS. Data collected at the Australian Synchrotron SAXS/WAXS beamline were monodisperse, with no apparent protein aggregation indicated by the linear fit in Guinier analyses (Fig. 2 (*g–i*) and Fig. S1). To obtain three-dimensional models of the protein variants from scattering intensities, we used the *ab initio* bead model approach performed in DAMMIF. At first glance, there appears to be a level of heterogeneity in the presented models (Fig. 2 (*g–i*) and Fig. S1), which is expected following computational modeling that is based on 10 independent simulations with the final model serving as a consensus of these. However, overall, all models grossly resemble the WT protein in solution (Fig. 2 (*g–i*) and Fig. S1), indicated by analogous maximum particle dimensions (D_{max}) of 105 Å across all mutants and comparable levels of compaction denoted by similar radius of gyration (R_g) values, ranging between ~31.1 and 32.2 Å (Table 1 and Table S1).

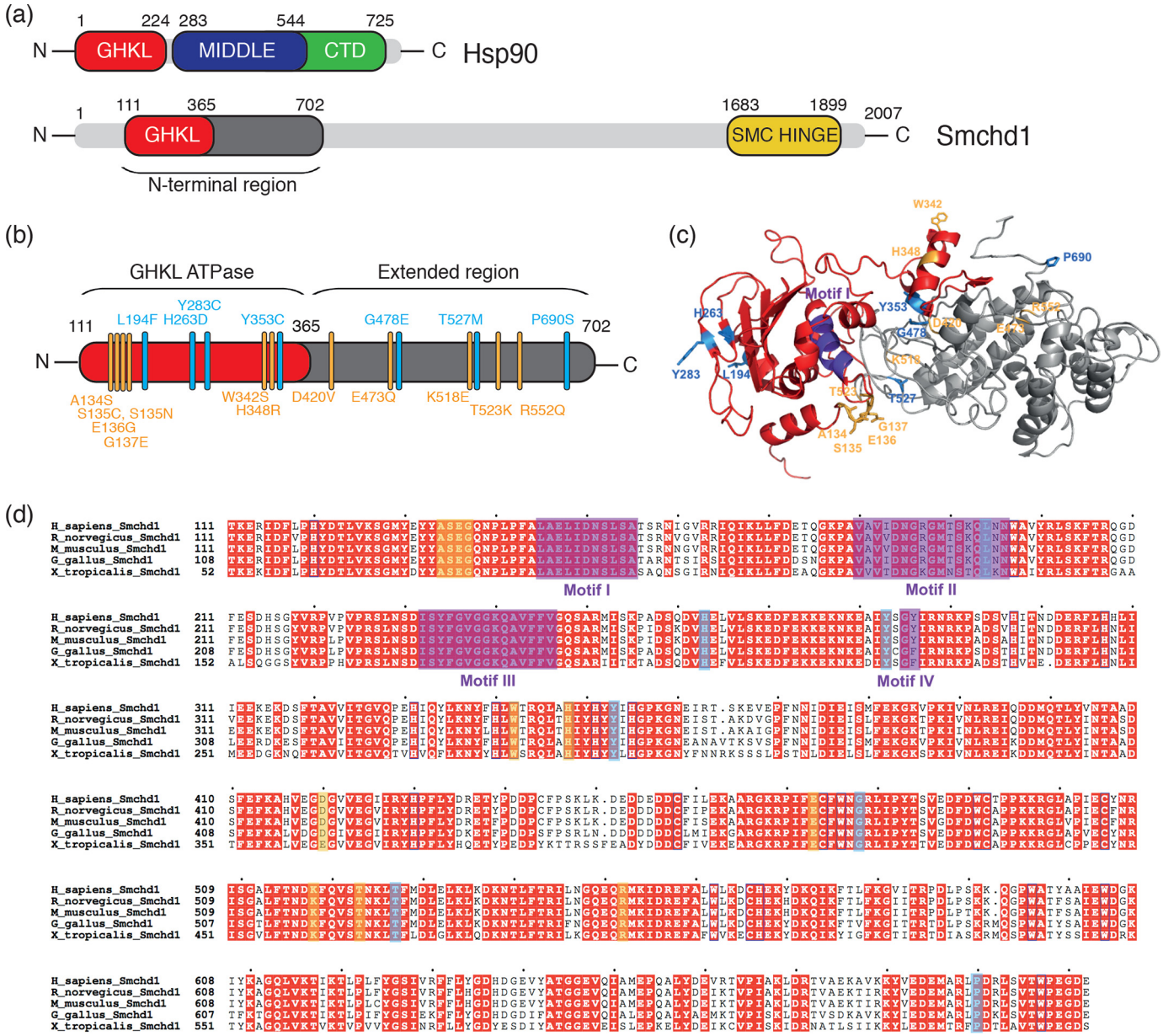

Figure 1. SMCHD1 mutations in FSHD2 and BAMS patients frequently occur within the GHKL-containing N-terminal region, which has structural homology to Hsp90. *a*, domain architectures of full-length Hsp90 comprising three domains (GHKL ATPase, middle, and C-terminal (*CTD*) domain) with domain boundaries indicated *above* as amino acids (*top*) and full-length SMCHD1 comprising the GHKL-containing N-terminal region (residues 111–702) and an SMC hinge domain (residues 1683–1899) (*bottom*). *b* and *c*, illustration of studied *SMCHD1* mutations associated with FSHD2 (*blue*) and BAMS (*yellow*) located within SMCHD1's N-terminal region, where the GHKL ATPase is *colored* in *red* and the extended region is shown in *gray*; depicted in *b* is the gene structure and in *c* a homology model of Smchd1's N-terminal region based on Hsp90, indicating the catalytic motif I in *purple*. *d*, multiple-sequence alignment of Smchd1 (residues 111–702) orthologue sequences from *Homo sapiens*, *Rattus norvegicus*, *M. musculus*, *Gallus gallus*, and *Xenopus tropicalis*. Conserved residues are *colored* in *red*, whereas nonconserved residues are shown in *black*; the four GHKL motifs are highlighted in *purple*, and mutations associated with FSHD2 (*blue*) and BAMS (*yellow*) are indicated. The alignment was generated with ClustalW and ESPript version 3.0.

FSHD2-associated mutations suppress the in vitro ATPase activity of Smchd1

SMCHD1 mutations identified in both FSHD2 and BAMS cohorts affect highly conserved residues (Fig. 1*d*) across all subdomains. FSHD2 patients most commonly present with predominantly heterozygous missense mutations that can be found anywhere in the protein, followed by out-of-frame deletions and finally deletions of chromosomal regions encompassing *SMCHD1* (4, 5). The *SMCHD1* mutations co-segregate with a loss of *D4Z4* methylation as well as reduced SMCHD1 protein levels in patient fibroblasts, together strongly supporting a loss of function of SMCHD1 (4). To further examine the effect of FSHD2-associated *SMCHD1* missense mutations, we subjected WT recombinant Smchd1(111–702) and counterparts harboring the FSHD2 variants, L194F, H263D, Y283C, Y353C, G478E, T527M, and P690S, to an *in vitro* fluorescence polarization–based ATPase assay. Our assays revealed that six of seven tested mutants display a loss of catalytic activity, whereas one showed no change (Fig. 3, *a–h* and *u*). Two mutations, Y353C and G478E, were the most severely affected and retained only ~3

and ~2% of WT protein catalytic activity, respectively. Despite exhibiting a loss of catalytic activity, the two mutants retained a WT-like thermal stability, indicating that the altered activity cannot be attributed to protein misfolding or instability. Remarkably, these residues appear to be located in spatial proximity to each other in a structural homology model based on Hsp90; both are surface-exposed and reside between the GHKL domain (residues 111–365) and the extended region (residues

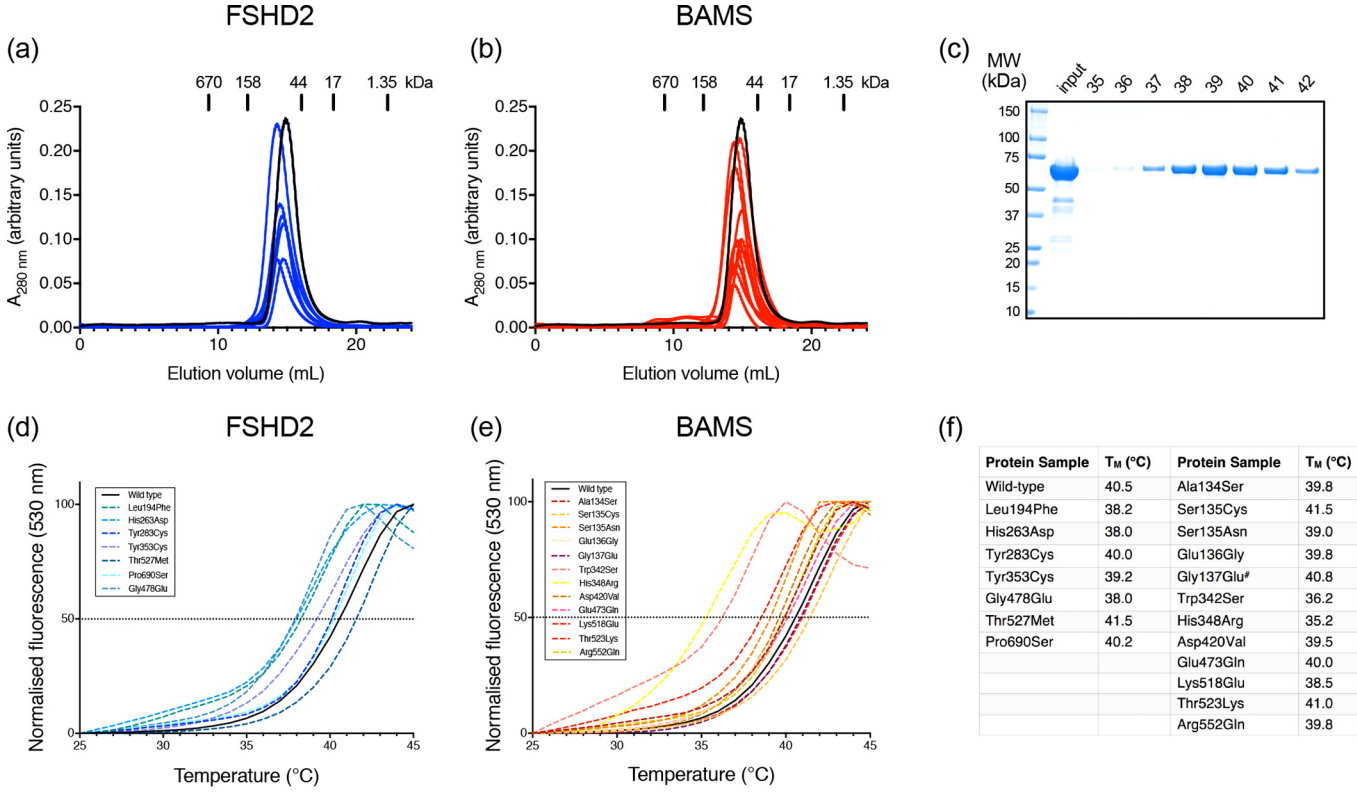

(f)

Protein Sample	T_M (°C)	Protein Sample	T_M (°C)
Wild-type	40.5	Ala134Ser	39.8
Leu194Phe	38.2	Ser135Cys	41.5
His263Asp	38.0	Ser135Asn	39.0
Tyr283Cys	40.0	Glu136Gly	39.8
Tyr353Cys	39.2	Gly137Glu#	40.8
Gly478Glu	38.0	Trp342Ser	36.2
Thr527Met	41.5	His348Arg	35.2
Pro690Ser	40.2	Asp420Val	39.5
		Glu473Gln	40.0
		Lys518Glu	38.5
		Thr523Lys	41.0
		Arg552Gln	39.8

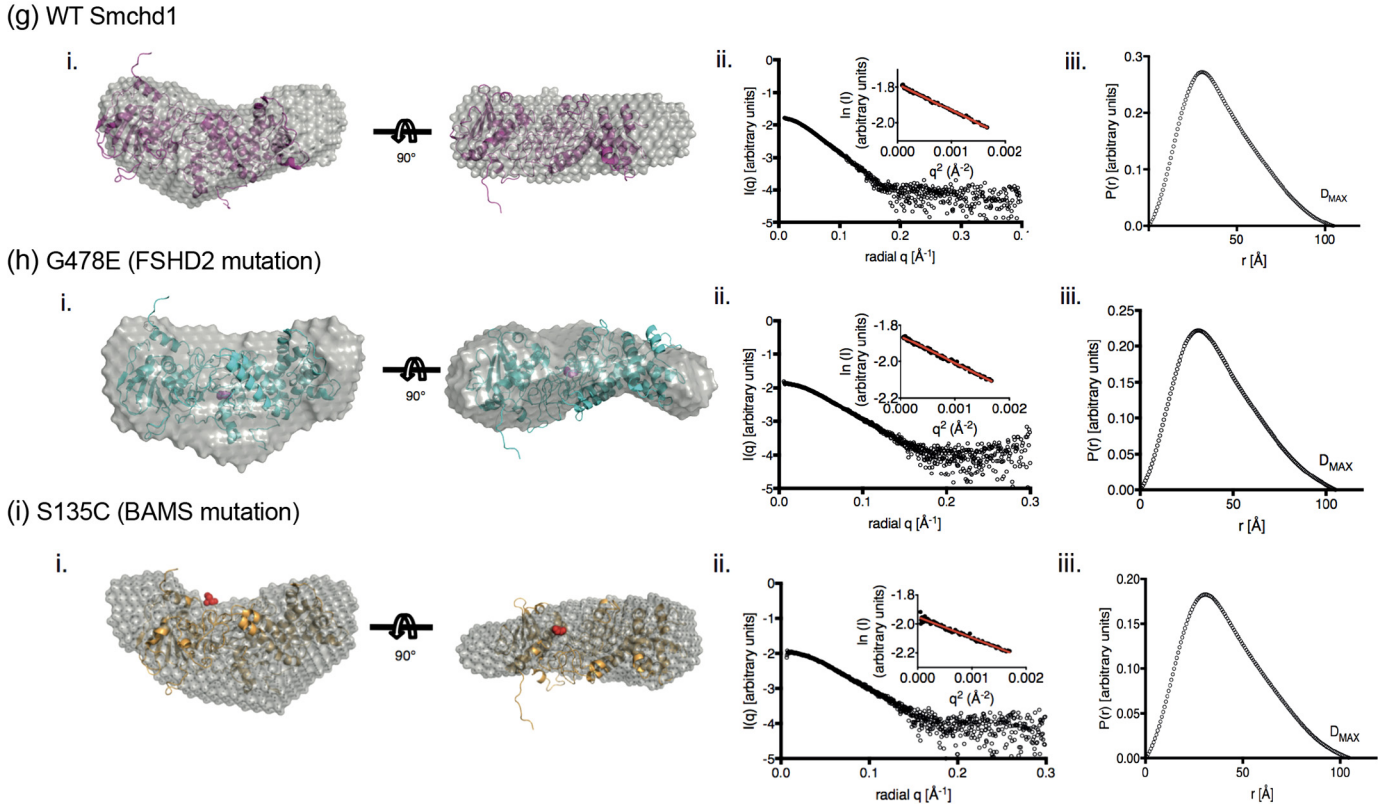

Table 1
Summary of studied *Smchd1* mutations

Mutant	Position	R_g[a]	D_{MAX}[a]	T_m	Percentage of WT activity	Craniofacial defects in *Xenopus* development
		Å	*Å*	*°C*	*%*	
FSHD						
WT[b]		32.3 ± 0.2	105	40.5	100	No (Ref. 6 and present study)
L194F	Core ATPase (motif II)	33.2 ± 0.2	105	38.2	48.9	Not tested
H263D	Core ATPase	32.8 ± 0.2	105	38.0	34.9	Not tested
Y283C	Core ATPase	32.5 ± 0.2	105	40.0	105	Not tested
Y353C	C-terminal to core ATPase	32.8 ± 0.1	105	39.2	3.2	No (Ref. 6 and present study)
G478E	C-terminal to core ATPase	32.8 ± 0.3	105	38.0	2.07	Not tested
T527M	C-terminal to core ATPase	32.4 ± 0.3	105	41.5	71.4	Not tested
P690S	Extended region	32.6 ± 0.2	105	40.2	58.9	Not tested
BAMS						
A134S	Core ATPase adjacent to motif I	Not tested	Not tested	39.8	129	Yes (6)
S135C	Core ATPase adjacent to motif I	32.5 ± 0.4	105	41.5	315	Not tested
S135N	Core ATPase adjacent to motif I	Not tested	Not tested	39.0	97.0	Not tested
E136G	Core ATPase adjacent to motif I	Not tested	Not tested	39.8	146	Not tested
G137E[c]	Core ATPase adjacent to motif I	Not tested	Not tested	40.8	150	Yes
W342S	C-terminal to core ATPase	32.2 ± 0.1	105	36.2	67.5	Yes
H348R	C-terminal to core ATPase	Not tested	Not tested	35.2	110	Yes (6)
D420V	Extended region	32.6 ± 0.2	105	39.5	88.7	Yes (6)
E473Q	Extended region	Not tested	Not tested	40.0	71.5	Not tested
K518E	C-terminal to core ATPase	32.2 ± 0.1	105	38.5	171	Not tested
T523K	C-terminal to core ATPase	32.7 ± 0.3	105	41.0	84.9	Not tested
R552Q	Extended region	32.1 ± 0.1	105	39.8	106	Yes

[a] R_g and D_{max} were derived from GNOM analysis of SAXS data and presented in their entirety in Table S1.
[b] WT SAXS data were reported previously (20) and are included for comparison.
[c] Mutation identified in both a BAMS and an FSHD2 patient.

365–702) (Fig. 1*c*). The FSHD2-associated mutant, T527M, is likewise located in proximity to this region (Fig. 1*c*); however, it induces less drastic changes in ATPase function, as it retains ~70% of WT catalytic activity (Fig. 3*u*). Overall, the predicted region between the two subdomains, the GHKL fold and the extended region, appears to be composed of residues with functional importance.

The FSHD2 mutant, H263D, also exhibited a marked reduction in ATP turnover, with ~35% of the WT protein activity (Fig. 3*u*). Y283C, also FSHD-associated, neighbors His-263 in the ATPase structural model (Fig. 1*c*) yet interestingly shows no discernible change in ATPase activity in this context (Fig. 3*u*). The reduction in the catalytic activity of H263D may be attributed to the properties of the substituted amino acid. Histidine is a positively charged residue at physiological pH, whereas aspartic acid is negatively charged. Additionally, His-263 is immediately adjacent to another negatively charged residue, a glutamic acid, Glu-264 (Fig. 1*d*). This substitution therefore results in two neighboring negatively charged residues that may introduce an electrostatic repulsion, potentially altering the local structure. From the homology model based on the Hsp90 structure, Smchd1 residues His-263 and Tyr-283 are positioned in a region that corresponds to its most N-terminal β-strand, which has been recognized to participate in a domain-swapping event upon N-terminal dimerization of two Hsp90 protomers (30, 31). Hence, if this phenomenon is conserved between the two proteins, localized mutations in this region may prevent domain swapping and consequently homodimerization from occurring in the full-length Smchd1, potentially accounting for loss of function in these two mutants in an *in vivo* context.

Enzymes belonging to the GHKL-ATPase family contain four conserved sequence motifs (Fig. 1*d*) important for maintaining the structural integrity of the ATP-binding site (19). Two of these, motifs II and IV, surround the adenine moiety of ATP, and notably motif II harbors Leu-194, which is mutated to Phe in an FSHD2-associated mutation. Introduction of the bulkier Phe generated a recombinant protein with ~50% of WT protein activity (Fig. 3*u*), which may arise from steric effects proximal to the predicted active site comprising the catalytic motif I (Fig. 1*c*). On the surface of the model, toward the C-terminal end of this construct, lies the P690S mutation (Fig. 1*c*). Proline is distinctive for its conformational rigidity; hence, this substitution may alter the local protein fold, in turn affecting protein function, as the recombinant protein appears to sup-

Figure 2. Protein purification and thermal stability analyses of studied Smchd1 N-terminal region mutants. *a* and *b*, SEC profiles of FSHD2-associated (*blue*) (*a*) and BAMS-associated (*red*) (*b*) recombinant proteins, indicating absorbance at 280 nm (*y* axis, arbitrary units) and elution volume (*x* axis, milliliters), obtained via a Superdex 200 10/30 column. WT Smchd1 elution is shown in *black* as a comparison in both *a* and *b*. Elution times of molecular mass markers are indicated *above* in kDa. *c*, representative Coomassie-stained 4–12% (w/v) reducing SDS-polyacrylamide gel indicating collected fractions following SEC and the high purity of protein obtained. Molecular mass markers are shown on the *left*. *d* and *e*, TSA results of all studied FSHD2 (*d*) and BAMS (*e*) mutants, indicating fluorescence intensity (*y* axis, 530 nm), temperature (*x* axis, °C) and the melting temperature (T_m) at which 50% protein has denatured as a *horizontal dotted line*. The TSA plots are representative of two independent experiments for each mutant. *f*, *table* summary. *g–i*, *ab initio* bead models of representative FSHD2 and BAMS mutants derived from in-solution SAXS data indicate a conserved structural topology. WT Smchd1 (*g*) was analyzed previously (20) and used to compare with newly acquired analyses of the G478E FSHD2 (*h*) and S135C BAMS (*i*) mutants. *Ab initio* models (*panels i*) are represented as a *gray surface*, superimposed with the predicted structural model of Smchd1's N-terminal region based on the Hsp90 crystal structure (PDB code 2CG9), shown in *cyan* for WT and FSHD-associated mutants and in *yellow* for BAMS-associated mutants. Affected residues are depicted as *red spheres* across all models. Images were obtained via PyMOL. *Panels ii* depict scattering profiles, with intensity of scattered X-rays, $I(q)$, as a function of momentum transfer, q, in $Å^{-1}$, showing *inset* Guinier plots for the corresponding mutants, where linearity indicates monodisperse particles. The R_g and initial scattering intensity ($I(0)$) were approximated from the Guinier plots via the software PRIMUS. *Panels iii* indicate the pair-distribution functions, $P(r)$, obtained via Fourier transformations of the scattering intensity data (*panels ii*), via the software GNOM. R_g and D_{max} (maximum dimension) values were also calculated from the $P(r)$ analyses. Calculated values are summarized in Table 1 and presented in their entirety in Table S1. SAXS data and analyses for seven FSHD2 and seven BAMS mutants are presented in Fig. S1.

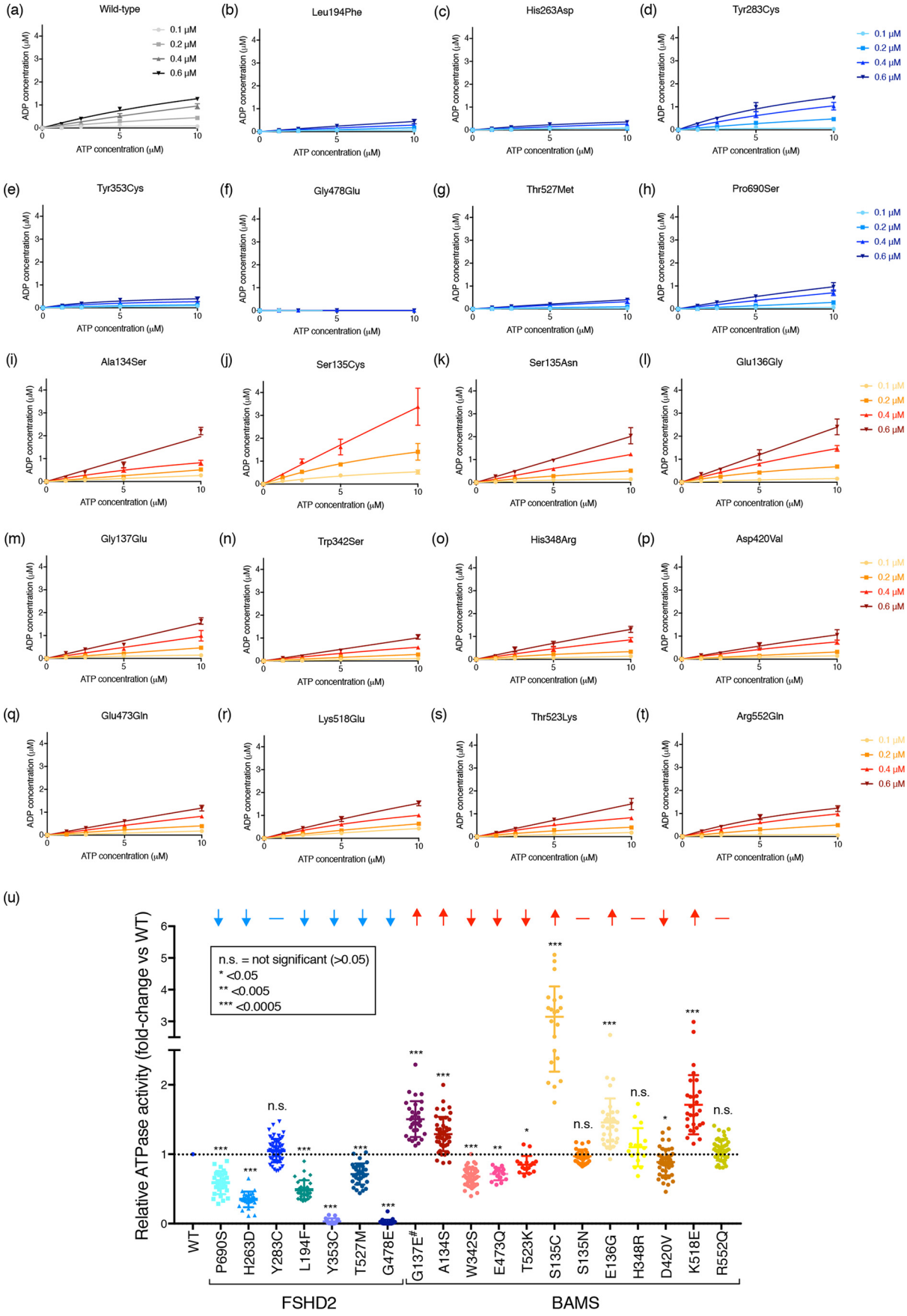
(a) Wild-type
(b) Leu194Phe
(c) His263Asp
(d) Tyr283Cys
(e) Tyr353Cys
(f) Gly478Glu
(g) Thr527Met
(h) Pro690Ser
(i) Ala134Ser
(j) Ser135Cys
(k) Ser135Asn
(l) Glu136Gly
(m) Gly137Glu
(n) Trp342Ser
(o) His348Arg
(p) Asp420Val
(q) Glu473Gln
(r) Lys518Glu
(s) Thr523Lys
(t) Arg552Gln
0.1 µM
0.2 µM
0.4 µM
0.6 µM
ADP concentration (µM)
ATP concentration (µM)
(u)
Relative ATPase activity (fold-change vs WT)
n.s. = not significant (>0.05)
* <0.05
** <0.005
*** <0.0005
WT
P690S
H263D
Y283C
L194F
Y353C
T527M
G478E
G137E#
A134S
W342S
E473Q
T523K
S135C
S135N
E136G
H348R
D420V
K518E
R552Q
FSHD2
BAMS

press the mutant's catalytic activity to ~60% of WT (Fig. 3*u*). Attempts to study two further FSHD2-associated mutants, R479P and V615D, were thwarted by the impact of these substitutions on protein stability, which prevented preparation of sufficient protein for biochemical analysis, raising the prospect that such instability may account for their effect on SMCHD1 in disease.

BAMS-associated mutations exhibit varied changes in ATPase activity, with hot spot residues for gain-of-function adjacent to the catalytic motif I

The occurrence of exclusively missense *SMCHD1* mutations in BAMS is consistent with a gain-of-function phenotype, and their restricted location within the protein's N-terminal GHKL-containing region suggests a propensity for an altered catalytic activity. Our previous studies indicated that a gain of ATPase activity arises from the BAMS-associated A134S, S135C, and E136G mutants (6). Here, we expanded our analysis to examine the ATPase activities of the additional BAMS-associated mutants, S135N, G137E, W342S, H348R, D420V, E473Q, K518E, T523K, and R552Q. Of these mutants, G137E and K518E showed an increase in catalytic activity; S135N, H348R, and R552Q exhibited catalytic rates comparable with WT protein; and W342S, E473Q, T523K, and D420V showed a mild decrease in activity. Combined with our earlier studies, overall, five of the 12 studied BAMS-associated mutants showed an increased catalytic activity, three showed no change relative to WT protein, and four exhibited a mild reduction in catalytic ability, albeit to a lesser extent than observed in FSHD-associated mutants (Fig. 3, *i*–*u*).

These studies suggest the existence of a gain-of-function hot spot region, comprising residues 134–137, located adjacent to catalytic motif I and pointing toward the outer protein surface based on the homology model of Hsp90 (Fig. 1*c*). Mutations A134S, S135C, E136G, and G137E all result in an enhanced catalytic activity of the recombinant proteins, displaying increases by ~30, 300, 50, and 50%, respectively, relative to the WT counterpart (Fig. 3*u*). Despite affecting the same residue, the substitution mutation S135N shows no difference in ATPase activity compared with the WT protein, indicating a particular role of the introduced cysteine. Whereas cysteine often participates in disulfide bond formation, our SEC and SAXS data rule out a potential homodimerization event of the S135C recombinant protein, as it retains a monomeric state (Fig. 2*b* and Fig. S1*o*), and our ATPase assays are performed under reducing conditions. Thus, the effect of Cys substitution most likely arises from the properties of the Cys side chain, possibly through loss of key hydrogen bonds mediated by Ser-135 or by introduction of a nonnative intramolecular disulfide. Based on these results, it appears that the conserved residues 134–137 are favorably positioned to enhance the catalytic function of Smchd1's N-terminal region.

The W342S variant showed the greatest decrease in ATPase activity within the BAMS cohort, exhibiting ~67% of WT Smchd1 ATP turnover (Fig. 3*u*). Moreover, this mutant displays a significant reduction in thermal stability, with a T_m of 36.2 °C compared with 41 °C exhibited by WT protein (Table 1). In the structural model of the Smchd1 ATPase domain, Trp-342 lies within the same helix as His-348, which is mutated to Arg in a BAMS patient. Like W342S, H348R exhibited a marked reduction in thermal stability, with a T_m of 35.2 °C (Fig. 2, *e* and *f*). Interestingly, this mutant appears to retain a WT-like catalytic function (Fig. 3*u*). Based on their positioning, these data indicate that the two mutations may perturb local or interdomain contacts, compromising the global protein stability (Fig. 1*c*). The altered protein stability makes interpreting the decreased or unchanged catalytic activity challenging.

A subset of BAMS-associated mutations affect residues located within the extended ATPase region of the construct, away from the catalytic pocket (Fig. 1, *b* and *c*). One of these, E473Q, displays a relatively mild effect on ATPase function, as it exhibits a ~30% decrease, whereas another, R552Q, shows no difference relative to WT ATPase (Fig. 3*u*). The D420V and T523K mutants are proximally located in the structural model (Fig. 1, *b* and *c*), and similarly exhibit only marginal effects on catalytic activity, as they retain ~89 and 85% of WT protein activity (Fig. 3*u*). The only tested mutation that appears to enhance ATPase function that is not located within the gain-of-function hot spot region is K518E. Like the BAMS-associated affected residues D420V, E473Q, T523K, and R552Q, Lys-518 is situated within the extended ATPase region of Smchd1 (Fig. 1*b*), and substitution from a positive to a negatively charged residue results in two neighboring negative charges, as indicated by the sequence alignment (Fig. 1*d*). This appears to favor a gain of ATPase function, as the mutant displays a ~1.7-fold increase in catalytic activity compared with WT protein (Fig. 3*u*). Within the Hsp90-based homology model, Lys-518 is positioned within the predicted interdomain region, where the most potent FSHD2-associated modifiers of catalytic activity also reside, again indicating an overall functional importance of this region (Fig. 1*c*).

It is worth noting that the *SMCHD1* mutation G137E is reportedly identified in both a BAMS and an FSHD patient,

Figure 3. *In vitro* ATPase analyses indicate FSHD-associated mutants display a loss of catalytic ability, whereas varied changes are observed across BAMS mutants. *a*–*t*, ATPase activity analyses of FSHD2-associated (*b*–*h*) and BAMS-associated (*i*–*t*) mutants, *alongside* representative WT-protein activity (*a*). Each graph indicates ATP concentration (*x* axis, μM), concentration of ADP produced (*y* axis, μM), and protein concentration (*right panels*), where measurements were performed in technical triplicates, and *error bars* represent S.D., with at least two independent experiments performed for each protein variant. Plots (*a*–*t*) depict individual experiments carried out at separate times, where WT protein was assessed within each assay (not shown), and the profile (*a*) serves as a representative result. ATPase analyses for mutants A134S, S135C, E136G, D420V, Y353C, and T527M were previously reported by Gordon *et al.* (6), with additional repetitions included in these studies. *u*, relative -fold change in ATPase activity (*y* axis) of all studied mutants compared with WT protein, where individual mutations are indicated (*x* axis), *alongside* overall changes in catalytic activity depicted by *overhead arrows* (FSHD2 in *blue*, BAMS in *red*) or a *horizontal line* if no significant change was apparent. G137E is indicated with a *number symbol*, as the mutation was reported in both a BAMS patient and an FSHD2 patient, yet we included it in the BAMS cohort for analysis purposes. -Fold change values were calculated by direct comparison of 16 points (four ATP and protein concentrations tested per mutant) obtained for each mutant, compared with the corresponding 16 values obtained for the WT protein within each assay performed. Statistical analysis was carried out using the Wilcoxon matched-pairs signed-rank test, additionally applying a correction for multiple testing. *p* values were obtained, as indicated in the *outlined box*. See *u* to comparing ATPase activity of mutants to WT protein.

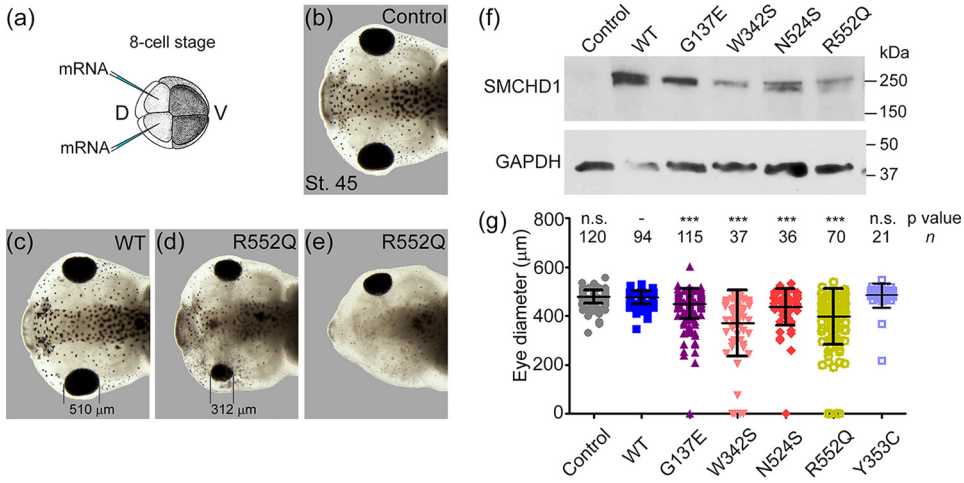

Figure 4. BAMS-associated mutant forms of SMCHD1 result in a decreased eye diameter in *X. laevis*. *a*, synthesized mRNA encoding full-length human SMCHD1 was injected into the two dorsal animal blastomeres at the 8-cell stage to target the head structures. *b–e*, representative images of stage 45 tadpoles that were uninjected (*b*), injected with WT mRNA (*c*), or injected with R552Q mRNA (*d–e*). *f*, Western blotting showing that all injected mRNAs produced full-length SMCHD1 protein. Y353C mRNA has been tested previously (6). *g*, measurements of eye diameter of tadpoles show that all BAMS-associated mutants cause a significant reduction in eye size. *n* indicates the number of embryos analyzed; data are shown as means ± S.D. (*error bars*), and *p* values were calculated by one-way ANOVA followed by Dunn's post-test. *n.s.*, not significant; ***, $p < 0.001$.

where the latter patient lacks critical information relating to *D4Z4* methylation status (7, 27). We provide supporting evidence of this mutation being exclusively BAMS-associated, as the recombinant protein exhibits a ~1.5-fold increase in ATP hydrolysis compared with WT Smchd1 (Fig. 3*u*) and retains a native melting temperature (T_m) of 41 °C, representative of a stable protein (Fig. 2, *e* and *f*). The G137E mutant therefore appears discordant with FSHD2-associated mutations where loss-of-function of SMCHD1 has been established as a key contributing factor. Whereas results from our biochemical assay provide valuable information, the challenge remains in determining whether these variants can be interpreted as disease-causing mutations or simply SNPs, which is clearly of diagnostic importance for patients.

BAMS-associated mutations result in a smaller eye diameter in Xenopus

We previously used *Xenopus* eye formation as a relevant *in vivo* model in which to study the functional effects of SMCHD1 mutations (6). This model organism was chosen because mRNA injection into *Xenopus* embryos affords a rapid *in vivo* model in which to study the effects of overexpression of specific mutant or WT transcripts. To mimic the endogenous expression pattern of SMCHD1 in the head region, mRNA was injected into the two dorsal animal blastomeres of the eight-cell embryo (Fig. 4*a*). We reported previously that overexpression of the BAMS-associated mutations, A134S, H348R, and D420V, resulted in a smaller eye diameter, similar to the microphthalmia phenotype observed in BAMS patients, whereas overexpression of the FSHD2-associated mutation Y353C did not (5). Here, to complement our biochemical assays, we tested BAMS-associated mutations G137E, W342S, N524S, and R552Q for their effect on *Xenopus* eye formation. For all four of these mutants, we observed a smaller and more variable eye diameter in *Xenopus* embryos injected with the mRNA encoding the mutant form of SMCHD1, compared with embryos injected with the WT *SMCHD1* mRNA, consistent with our earlier studies (Fig. 4, *b–g*). In severe cases, the embryos display anophthalmia (Fig. 4*e*). Injected embryos were verified to be expressing into full-length human SMCHD1 protein (Fig. 4*f*). Importantly, G137E, the mutation reported in both a BAMS patient and a patient diagnosed with FSHD2, results in a decreased eye diameter, providing additional support for the idea that the mutation causes BAMS and that the patient carrying the G137E substitution may in fact suffer from a molecularly unrelated but phenotypically similar muscular dystrophy, such as limb girdle muscular dystrophy (32).

Discussion

The rare outcome of both loss- and gain-of-function mutations in the same protein-coding gene leading to two distinct conditions has sparked great interest in the investigation of SMCHD1's molecular function. We previously reported *de novo* heterozygous missense mutations restricted to the ATPase domain of *SMCHD1* as causative of BAMS (6), as opposed to FSHD2 patients, who have been established to harbor loss-of-function mutations that contrastingly occur throughout the gene (4). Our *in vitro* studies examining the ATPase activity of BAMS-associated mutants showed that several exhibit an enhanced catalytic activity, whereas the use of *Xenopus laevis* embryos revealed dose-dependent craniofacial anomalies in the models overexpressing BAMS-associated SMCHD1 mutants, with measurable reductions in eye diameter that partially recapitulate the BAMS phenotype in human patients. A similar phenotype was achieved upon injection of a higher quantity of WT SMCHD1 (6), strongly suggesting that these mutations behave as gain-of-function alleles rather than loss-of-function ones, as observed in the case of FSHD2. Shaw *et al.* (7) challenged our findings, as they reported that the knockdown or CRISPR F0 knockout of *smchd1* in zebrafish resulted in a small-eye phenotype, yet this effect could not be reproduced in the mouse upon the introduction of BAMS-associated mutations. The inability to recapitulate BAMS craniofacial defects by introduction of patient mutations within

Smchd1 in mice is perhaps not surprising, considering the functional redundancy apparent in rodent compared with human craniofacial development (33). Furthermore, FSHD2 is also challenging to model in mice, due to intrinsic differences in mouse and human genomic structures. Specifically, mice lack the same genomic arrangement of *Dux4* within a macrorepeat array. Thus, the defects in SMCHD1 silencing of the *D4Z4* repeat encoding the DUX4 transcription factor that underlie FSHD are not recapitulated in mouse models. Consequently, the capacity of ectopic expression of mutant SMCHD1 proteins in the *Xenopus* oocyte model to induce craniofacial developmental defects that resemble the human BAMS phenotype provides a valuable platform for examining whether patient *SMCHD1* mutations are loss- or gain-of-function. Building on our earlier studies (6), here we expanded our studies to examine additional BAMS-associated mutations, with our results consistent with our previous model.

Using recombinant proteins, we observed the recurrent loss of ATPase activity across FSHD2-associated mutants, which correlates with the established loss of overall SMCHD1 function *in vivo* in FSHD2 patients. The lack of high-resolution structural data on Smchd1 has made it challenging to fully understand its molecular function; however, our homology model of its extended ATPase domain based on Hsp90 allowed us to interpret possible effects of disease-associated mutations in *SMCHD1*. We can speculate that some mutations may directly or indirectly affect ATP binding and hydrolysis, depending on their position within the Smchd1 extended ATPase model. Using SAXS, we found that the overall protein shape and compactness appeared very similar across all mutants studied, indicating that the recombinant proteins retain appropriate folding and topology. It is therefore likely that the introduced mutations may only alter the local protein structure, which cannot be captured via SAXS, yet in most cases appear sufficient to affect the protein's catalytic function. We can speculate that some mutations may directly or indirectly affect ATP binding and hydrolysis, whereas others may alter the structure of the ATP-binding site, depending on their position within the Smchd1 extended ATPase model. Taken together, these results indicate that ATP hydrolysis may be necessary for SMCHD1's repressive function at *D4Z4* repeats. However, we cannot rule out the possibility that some of the mutants may alter Smchd1's function in an ATP-independent manner. A more detailed understanding of mutation-induced changes awaits determination of a high-resolution structure of SMCHD1's ATPase domain. What also remains to be investigated is the function of the catalytic activity exerted by the ATPase domain and whether this indeed fuels a conformational change in SMCHD1 required for chromatin interaction or manipulation, as hypothesized.

The recurrence of both FSHD- and BAMS-associated mutations within the region predicted in our model to lie between the core GHKL ATPase domain and its C-terminal extension and their impact on Smchd1's ATPase activity strongly support the functional importance of this region. In Hsp90, the N-terminal, middle, and C-terminal domains are joined by long, charged, flexible linkers that mediate communication and regulation of ATPase activity and allow the dimer to undergo dramatic conformational rearrangements (34). It is also worth noting that mutated residues in Hsp90's corresponding middle and C-terminal subdomains have been previously demonstrated to alter Hsp90 activity, such as Arg-380 (35), Ala-577 (36), and Ala-587 (37). Considering the requirement of Smchd1's extended ATPase region for the production of stable N-terminal region protein (20), a regulatory effect upon Smchd1's catalytic activity may likewise be inferred for this region. Mutations in the vicinity may therefore perturb potential interactions between Smchd1's ATPase extended region, corresponding to the middle and N-terminal domains, respectively, in Hsp90, and the ATPase domain itself, leading to analogous alterations in catalytic activity.

Our data revealed varied effects on catalytic activity among the BAMS-associated mutants studied. There appears to be a hot spot region for gain-of-function mutations (A134S, S135C, E136G, and G137E) located adjacent to the catalytic motif I and toward the outer protein surface. Based on their proximity to catalytic residues, we speculate that these substitutions may modulate ATP interaction or alter the local structure toward a preferentially active conformation. Two BAMS variants, W342S and H348R, exhibited reduced thermal stability relative to WT protein in the context of the extended ATPase domain. Consistent with these substitutions impacting protein stability and expression levels in the context of full-length protein, W342S SMCHD1 exhibited reduced protein levels in *Xenopus* embryos upon mRNA injection. Two particularly interesting mutations within the BAMS cohort, S135C and S135N, occur at the same residue within the gain-of-function hot spot region yet show markedly different effects upon the catalytic activity of Smchd1. S135C displays a 3-fold increase in ATPase catalytic activity relative to WT protein, whereas S135N retains a WT-like activity. Our SEC and SAXS data rule out a potential dimerization event; hence, the substitution to cysteine may therefore affect ATP binding or help stabilize the tertiary structure to potentially induce a constitutively active conformation. A detailed understanding of the effects of Ser-135 substitutions on SMCHD1 ATPase activity awaits high-resolution structural information.

To assess the function of BAMS-associated *SMCHD1* mutations in craniofacial development, our earlier data demonstrate the utility of an *in vivo* functional assay in *Xenopus* embryos. In our previous work, injection of *SMCHD1* mRNA encompassing the mutations A134S, H348R, or D420V each correlated with a reduction in eye diameter in the subjected tadpoles. Here, we have extended these data to consider four further BAMS-associated *SMCHD1* mutations and again found that all mutants resulted in a smaller eye diameter compared with *Xenopus* embryos injected with the same amount of WT *SMCHD1* mRNA. These additional data are entirely consistent with our earlier data but importantly highlight that G137E, a mutation found in both a BAMS patient and an FSHD2 patient, exhibits a gain-of-function phenotype both in this *in vivo* model and in our biochemical assay.

The discrepancies observed in the *in vitro* catalytic changes across different BAMS mutants compared with their universal effect on *Xenopus* eye formation indicate that these mutants may behave differently in an *in vivo* context. The full-length

protein may be required to faithfully recapitulate the mutation-associated changes. We are particularly interested to test the catalytic changes of these mutations in the context of full-length Smchd1; however, the large size of Smchd1 has made addressing this question technically very challenging. Based on our current knowledge of Smchd1's structural arrangement, we have previously shown that it homodimerizes at the C-terminal hinge domain (17), similar to canonical SMC protein members, whereas the N-terminal GHKL-containing protein is found as a monomer in solution (20). Across several other GHKL proteins, such as Hsp90 and DNA gyrase, the dimerization of ATPase domains occurs as part of their functional cycle (19, 38, 39). It is therefore possible that Smchd1's GHKL domains also dimerize in the context of the full-length protein, driven by the C-terminal hinge domains, which may impact catalytic rates in the context of full-length SMCHD1 *in vivo*. Additionally, *in vivo*, there is additional complexity governing SMCHD1 activity, including post-translational modifications of SMCHD1 itself; the presence of interacting proteins or scaffolds, such as HBiX/Lrif (21, 40); and the effect of SMCHD1 substrates, such as nucleic acids and chromatin. A complete understanding of the effects of SMCHD1 substitutions in disease may therefore rely on future studies in the context of the full-length protein as well as in an *in vivo* context, where potential interacting partners or post-translational modifications may further alter its function.

Our principal findings suggest that a decreased catalytic activity of SMCHD1 may contribute to disease in FSHD2 patients, whereas the potential gain-of-function phenotype observed in BAMS-associated mutants reveals the possibility of specifically targeting active or allosteric sites in the extended ATPase domain to activate FSHD2-compromised SMCHD1. Of particular interest are small-molecule compounds that can increase SMCHD1's catalytic efficiency in individuals who are at high risk or in the early stages of developing FSHD2 in anticipation of preventing further muscle cell death. Our studies reported here suggest a potential region beyond the active site that could be targeted by such activator molecules. Furthermore, uncovering the role of SMCHD1 in nasal development, and hence unraveling the underlying cause of the rare condition, BAMS, remains of enormous interest.

Materials and methods

PCR-mediated site-directed mutagenesis

The Smchd1 N-terminal region (amino acids 111–702) was PCR-amplified from a *Mus musculus* Smchd1 template as described previously (20), and mutations were introduced by oligonucleotide-directed mutagenesis (sequences shown in Table S2). PCR products bearing oligonucleotide-encoded BamHI 5′ and EcoRI 3′ overhangs were restriction-digested and ligated into the pFastBac Htb vector (Life Technologies), and bacmids were prepared using the Bac-to-Bac system, as described previously (41). Insert sequences were verified by Sanger sequencing (Micromon, Monash).

Sf21 insect cell culture and protein expression

Sf21 insect cells were cultivated in Insect-XPRESS protein-free insect cell medium with L-glutamine (Lonza) in suspension at 27 °C, shaking at 130 rpm. Transfections were performed as outlined in the Bac-to-Bac protocol (Life Technologies, Inc.) (41). For large-scale protein expression, 0.5-liter cell cultures were grown in 2.8-liter Fernbach flasks, shaking at 90 rpm, 27 °C to a density of 3.0–3.5 $\times$ 10^6 cells/ml before infection with an empirically defined ratio of P2 virus for optimal protein yield. 48 h following infection, cell pellets were harvested by centrifugation at 500 $\times$ *g* for 5 min at room temperature and snap-frozen in liquid nitrogen for storage at −80 °C.

ATPase domain purification

Harvested *Sf*21 insect cell pellets were resuspended in lysis buffer (0.5 M NaCl, 20 mM Tris, pH 8, 20% glycerol, 10 mM imidazole, pH 8, 0.5 mM TCEP, 2 mM Na_3VO_4), using 25 ml of lysis buffer supplemented with 2 mM phenylmethylsulfonyl fluoride and EDTA-free cOmplete Protease Inhibitor mixture (Roche Applied Science) per 500 ml of *Sf*21 cell culture pellet. Cells were lysed by sonication, and insoluble material was removed by centrifugation at 45,000 relative centrifugal force for 30 min at 4 °C before application to washed cOmplete His tag resin (Roche Applied Science). Supernatants were incubated with the resin for 60 min on rollers at 4 °C before the resin was pelleted at 1500 $\times$ *g* for 5 min at 4 °C and washed with wash buffer (0.5 M NaCl, 20 mM Tris, pH 8, 20% glycerol, 35 mM imidazole, pH 8, 0.5 mM TCEP). His_6-Smchd1(111–702) was eluted in elution buffer (0.5 M NaCl, 20 mM Tris, pH 8, 20% glycerol, 250 mM imidazole, pH 8, 0.5 mM TCEP), and the His_6 tag was cleaved by overnight incubation with tobacco etch virus protease at 4 °C. Cleaved protein was diluted in ion-exchange chromatography buffer A (25 mM Tris, pH 7.5, 0.5 mM TCEP) and further concentrated by centrifugal ultrafiltration to 1 ml for application to a MonoQ 5/50 GL column (GE Healthcare) pre-equilibrated with buffer A. Elution was performed with a 0–100% gradient of buffer B (500 mM NaCl, 25 mM Tris, pH 7.5, 0.5 mM TCEP) over 40 column volumes, at a flow rate of 0.8 ml/min. Fractions containing ATPase domain, as assessed by reducing SDS-PAGE with SafeStain staining, were concentrated and applied to a Superdex-200 10/30 GL column (GE Healthcare) equilibrated in SEC buffer (200 mM NaCl, 20 mM HEPES, pH 7.5, 5% glycerol). Fractions containing the N-terminal region of Smchd1 (~68 kDa) were identified via reducing SDS-PAGE analysis, pooled, and separated into aliquots and snap-frozen in liquid nitrogen.

Thermal stability assay (TSA)

25-μl reactions containing 0.25 mg/ml WT or mutant Smchd1(111–702) diluted in SEC buffer up to 10 μl, 14 μl of TSA buffer (150 mM NaCl, 20 mM Tris, pH 8.0, 1 mM DTT), and 1 μl of 1:30-diluted SYPRO Orange dye (Molecular Probes) were subjected to thermal denaturation on a Qiagen Rotor-Gene Q instrument on which the temperature was raised by 1 °C/min from 25 to 95 °C, and fluorescence readings were taken at each interval, detected at 530 nm.

ATPase assay

The Transcreener ADP^2 fluorescence polarization kit (BellBrook Labs, LLC) was used in a competitive fluorescence polarization assay that is based on the detection of ADP, using end-point measurements. Triplicate 10-μl reactions were set up in

low-level, black, 384-well plates, containing 7 μl of reaction buffer, 1 μl of recombinant Smchd1 N-terminal region protein at concentrations varying from 0.1 to 0.6 μM or SEC buffer control, 1 μl of nuclease-free water, and 1 μl of ATP substrate ranging from 1.25 to 10 μM or nuclease-free water control. Reactions were incubated at room temperature for 1 h in the dark before the addition of 10 μl of detection mix for a further 1-h incubation. Pilot experiments established 1-h incubation times as optimal for signal-to-noise, with data at this time point on the linear part of the curve across a 3.9–250 μM range of ATP concentrations at 0.1 and 0.2 μM protein (Fig. S2). Fluorescence polarization (mP) was measured using an Envision plate reader fitted with an excitation filter (620/40 nm), emission filters (688/45 nm) (s and p channels), and D658/fp688 dual mirror (PerkinElmer Life Sciences). Readings obtained from no-antibody controls (free tracer) were set as 20 mP as a normalization baseline for all reactions for the assay. The manufacturer's instructions were followed to estimate the amount of ADP present in each reaction, using a 12-point standard curve for each ATP substrate concentration. Resulting graphs were generated via GraphPad Prism version 6 software.

SAXS data collection and analysis

SAXS data were collected at the Australian Synchrotron SAXS/WAXS beamline using an inline gel filtration column. 55 μl at ~5 mg/ml of purified protein samples were loaded on the column (Superdex 200 5/150), which was pre-equilibrated with 200 mM NaCl, 20 mM HEPES, pH 7.5, 5% glycerol. Data were collected using a 1.5-mm glass capillary at 16 °C and a Pilatus detector (1M; 170 × 170 mm) under continuous flow in 2-s intervals. Diffraction data were processed via the beamline control software ScatterBrain, where two-dimensional intensity plots obtained from the SEC elution peaks were radially averaged, normalized, and subtracted from the buffer background.

Data analyses were performed with the ATSAS suite (42), initially using PRIMUS (43) for the Guinier analysis. The pair-distribution function ($P(r)$) analyses, used to determine the maximum dimension of the scattering particle (D_{max}), was computed by indirect Fourier transform using GNOM (42). Low-resolution envelope shapes were modeled using the *ab initio* software DAMMIF (42), building 10 independent models for each sample; these were further analyzed via DAMSEL (42). The most probable models were determined by the software DAMSUP (42), which was further adjusted to correspond to the experimentally determined excluded volume by DAMFILT (42). The final bead model obtained was superimposed with the predicted structure of Smchd1's N-terminal region, modeled using the crystal structure of Hsp90 (PDB code 2CG9), using SUPCOMB (42). The homology model of the N-terminal region of mouse Smchd1 (residues 111–702) was generated using the online server Phyre2 (44), as described previously (6), using the intensive modeling mode. The presented model exhibited the most extensive sequence coverage when aligned with the crystal structure of yeast Hsp90 (PDB code 2CG9), which we had previously shown to exhibit analogous topology to the Smchd1 extended N-terminal domain in solution by SAXS (20).

Xenopus eye formation assay

X. laevis were used according to guidelines approved by the Singapore National Advisory Committee on Laboratory Animal Research. Mutations were generated in pCS2+ SMCHD1-PC (5) by site-directed mutagenesis (Agilent). Mutagenesis primers are listed in Table S2. *SMCHD1* mRNA was transcribed with the mMESSAGE mMachine SP6 kit (Thermo Fisher) and column-purified. mRNA injection into *Xenopus* embryos and eye formation assays were performed essentially as described by Gordon *et al.* (6). Briefly, the two dorsal-animal blastomeres were injected at the 8-cell stage with a total of 240 pg of mRNA/embryo. Embryos were allowed to develop at room temperature until stage 45–46 (4 days postfertilization) and fixed. Eye diameter was measured using a Leica stereomicroscope with a DFC 7000T digital camera. For protein analysis, embryonic extracts were prepared by lysing Stage 12 embryos in CelLytic Express (Sigma) on ice, followed by centrifugation to remove yolk proteins. Extracts were analyzed by Western blotting with anti-SMCHD1 (Atlas HPA039441) and anti-GAPDH antibodies (clone 0411, Santa Cruz Biotechnology, Inc.).

Author contributions—A. D. G., K. C., S. X., B. R., M. E. B., and J. M. M. conceptualization; A. D. G., K. C., S. X., I. S. L., T. T. N. L., and M. E. B. formal analysis; A. D. G., K. C., S. X., W. D., I. S. L., T. T. N. L., and B. R. investigation; A. D. G. writing-original draft; K. C., I. S. L., M. E. B., and J. M. M. supervision; K. C., S. X., and I. S. L. methodology; K. C., S. X., M. E. B., and J. M. M. writing-review and editing; S. X., B. R., and J. M. M. funding acquisition.

Acknowledgment—We thank the Australian Synchrotron SAXS beamline staff for technical assistance.

References

1. Blewitt, M. E., Vickaryous, N. K., Hemley, S. J., Ashe, A., Bruxner, T. J., Preis, J. I., Arkell, R., and Whitelaw, E. (2005) An *N*-ethyl-*N*-nitrosourea screen for genes involved in variegation in the mouse. *Proc. Natl. Acad. Sci. U.S.A.* **102,** 7629–7634 CrossRef Medline
2. Blewitt, M. E., Gendrel, A. V., Pang, Z., Sparrow, D. B., Whitelaw, N., Craig, J. M., Apedaile, A., Hilton, D. J., Dunwoodie, S. L., Brockdorff, N., Kay, G. F., and Whitelaw, E. (2008) SmcHD1, containing a structural-maintenance-of-chromosomes hinge domain, has a critical role in X inactivation. *Nat. Genet.* **40,** 663–669 CrossRef Medline
3. Jansz, N., Chen, K., Murphy, J. M., and Blewitt, M. E. (2017) The epigenetic regulator SMCHD1 in development and disease. *Trends Genet.* **33,** 233–243 CrossRef Medline
4. Lemmers, R. J., Tawil, R., Petek, L. M., Balog, J., Block, G. J., Santen, G. W., Amell, A. M., van der Vliet, P. J., Almomani, R., Straasheijm, K. R., Krom, Y. D., Klooster, R., Sun, Y., den Dunnen, J. T., Helmer, Q., *et al.* (2012) Digenic inheritance of an SMCHD1 mutation and an FSHD-permissive D4Z4 allele causes facioscapulohumeral muscular dystrophy type 2. *Nat. Genet.* **44,** 1370–1374 CrossRef Medline
5. Larsen, M., Rost, S., El Hajj, N., Ferbert, A., Deschauer, M., Walter, M. C., Schoser, B., Tacik, P., Kress, W., and Müller, C. R. (2015) Diagnostic approach for FSHD revisited: SMCHD1 mutations cause FSHD2 and act as modifiers of disease severity in FSHD1. *Eur. J. Hum. Genet.* **23,** 808–816 CrossRef Medline
6. Gordon, C. T., Xue, S., Yigit, G., Filali, H., Chen, K., Rosin, N., Yoshiura, K. I., Oufadem, M., Beck, T. J., McGowan, R., Magee, A. C., Altmuller, J., Dion, C., Thiele, H., Gurzau, A. D., *et al.* (2017) *De novo* mutations in SMCHD1 cause Bosma arhinia microphthalmia syndrome and abrogate nasal development. *Nat. Genet.* **49,** 249–255 CrossRef Medline

7. Shaw, N. D., Brand, H., Kupchinsky, Z. A., Bengani, H., Plummer, L., Jones, T. I., Erdin, S., Williamson, K. A., Rainger, J., Stortchevoi, A., Samocha, K., Currall, B. B., Dunican, D. S., Collins, R. L., Willer, J. R., *et al.* (2017) SMCHD1 mutations associated with a rare muscular dystrophy can also cause isolated arhinia and Bosma arhinia microphthalmia syndrome. *Nat. Genet.* **49,** 238–248 CrossRef Medline
8. Hirano, T. (2002) The ABCs of SMC proteins: two-armed ATPases for chromosome condensation, cohesion, and repair. *Genes Dev.* **16,** 399–414 CrossRef Medline
9. Zuin, J., Dixon, J. R., van der Reijden, M. I., Ye, Z., Kolovos, P., Brouwer, R. W., van de Corput, M. P., van de Werken, H. J., Knoch, T. A., van IJcken, W. F., Grosveld, F. G., Ren, B., and Wendt, K. S. (2014) Cohesin and CTCF differentially affect chromatin architecture and gene expression in human cells. *Proc. Natl. Acad. Sci. U.S.A.* **111,** 996–1001 CrossRef Medline
10. Sofueva, S., Yaffe, E., Chan, W. C., Georgopoulou, D., Vietri Rudan, M., Mira-Bontenbal, H., Pollard, S. M., Schroth, G. P., Tanay, A., and Hadjur, S. (2013) Cohesin-mediated interactions organize chromosomal domain architecture. *EMBO J.* **32,** 3119–3129 CrossRef Medline
11. Lengronne, A., Katou, Y., Mori, S., Yokobayashi, S., Kelly, G. P., Itoh, T., Watanabe, Y., Shirahige, K., and Uhlmann, F. (2004) Cohesin relocation from sites of chromosomal loading to places of convergent transcription. *Nature* **430,** 573–578 CrossRef Medline
12. Hu, B., Itoh, T., Mishra, A., Katoh, Y., Chan, K. L., Upcher, W., Godlee, C., Roig, M. B., Shirahige, K., and Nasmyth, K. (2011) ATP hydrolysis is required for relocating cohesin from sites occupied by its Scc2/4 loading complex. *Curr. Biol.* **21,** 12–24 CrossRef Medline
13. Ganji, M., Shaltiel, I. A., Bisht, S., Kim, E., Kalichava, A., Haering, C. H., and Dekker, C. (2018) Real-time imaging of DNA loop extrusion by condensin. *Science* **360,** 102–105 CrossRef Medline
14. Soh, Y. M., Bürmann, F., Shin, H. C., Oda, T., Jin, K. S., Toseland, C. P., Kim, C., Lee, H., Kim, S. J., Kong, M. S., Durand-Diebold, M. L., Kim, Y. G., Kim, H. M., Lee, N. K., Sato, M., *et al.* (2015) Molecular basis for SMC rod formation and its dissolution upon DNA binding. *Mol. Cell* **57,** 290–303 CrossRef Medline
15. Diebold-Durand, M. L., Lee, H., Ruiz Avila, L. B., Noh, H., Shin, H. C., Im, H., Bock, F. P., Bürmann, F., Durand, A., Basfeld, A., Ham, S., Basquin, J., Oh, B. H., and Gruber, S. (2017) Structure of full-length SMC and rearrangements required for chromosome organization. *Mol. Cell* **67,** 334–347.e5 CrossRef Medline
16. Minnen, A., Bürmann, F., Wilhelm, L., Anchimiuk, A., Diebold-Durand, M. L., and Gruber, S. (2016) Control of Smc coiled coil architecture by the ATPase heads facilitates targeting to chromosomal ParB/parS and release onto flanking DNA. *Cell Rep.* **14,** 2003–2016 CrossRef Medline
17. Chen, K., Czabotar, P. E., Blewitt, M. E., and Murphy, J. M. (2016) The hinge domain of the epigenetic repressor Smchd1 adopts an unconventional homodimeric configuration. *Biochem. J.* **473,** 733–742 CrossRef Medline
18. Chen, K., Hu, J., Moore, D. L., Liu, R., Kessans, S. A., Breslin, K., Lucet, I. S., Keniry, A., Leong, H. S., Parish, C. L., Hilton, D. J., Lemmers, R. J., van der Maarel, S. M., Czabotar, P. E., Dobson, R. C., *et al.* (2015) Genome-wide binding and mechanistic analyses of Smchd1-mediated epigenetic regulation. *Proc. Natl. Acad. Sci. U.S.A.* **112,** E3535–E3544 CrossRef Medline
19. Dutta, R., and Inouye, M. (2000) GHKL, an emergent ATPase/kinase superfamily. *Trends Biochem. Sci.* **25,** 24–28 CrossRef Medline
20. Chen, K., Dobson, R. C., Lucet, I. S., Young, S. N., Pearce, F. G., Blewitt, M. E., and Murphy, J. M. (2016) The epigenetic regulator Smchd1 contains a functional GHKL-type ATPase domain. *Biochem. J.* **473,** 1733–1744 CrossRef Medline
21. Brideau, N. J., Coker, H., Gendrel, A. V., Siebert, C. A., Bezstarosti, K., Demmers, J., Poot, R. A., Nesterova, T. B., and Brockdorff, N. (2015) Independent mechanisms target SMCHD1 to trimethylated histone H3 lysine 9-modified chromatin and the inactive X chromosome. *Mol. Cell Biol.* **35,** 4053–4068 CrossRef Medline
22. Tawil, R., and Van Der Maarel, S. M. (2006) Facioscapulohumeral muscular dystrophy. *Muscle Nerve* **34,** 1–15 CrossRef Medline
23. van der Maarel, S. M., and Frants, R. R. (2005) The D4Z4 repeat-mediated pathogenesis of facioscapulohumeral muscular dystrophy. *Am. J. Hum. Genet.* **76,** 375–386 CrossRef Medline
24. Yao, Z., Snider, L., Balog, J., Lemmers, R. J., Van Der Maarel, S. M., Tawil, R., and Tapscott, S. J. (2014) DUX4-induced gene expression is the major molecular signature in FSHD skeletal muscle. *Hum Mol. Genet.* **23,** 5342–5352 CrossRef Medline
25. Geng, L. N., Yao, Z., Snider, L., Fong, A. P., Cech, J. N., Young, J. M., van der Maarel, S. M., Ruzzo, W. L., Gentleman, R. C., Tawil, R., and Tapscott, S. J. (2012) DUX4 activates germline genes, retroelements, and immune mediators: implications for facioscapulohumeral dystrophy. *Dev. Cell* **22,** 38–51 CrossRef Medline
26. de Greef, J. C., Lemmers, R. J., Camaño, P., Day, J. W., Sacconi, S., Dunand, M., van Engelen, B. G., Kiuru-Enari, S., Padberg, G. W., Rosa, A. L., Desnuelle, C., Spuler, S., Tarnopolsky, M., Venance, S. L., Frants, R. R., *et al.* (2010) Clinical features of facioscapulohumeral muscular dystrophy 2. *Neurology* **75,** 1548–1554 CrossRef Medline
27. Lemmers, R. J., Goeman, J. J., van der Vliet, P. J., van Nieuwenhuizen, M. P., Balog, J., Vos-Versteeg, M., Camano, P., Ramos Arroyo, M. A., Jerico, I., Rogers, M. T., Miller, D. G., Upadhyaya, M., Verschuuren, J. J., Lopez de Munain Arregui, A., van Engelen, B. G., *et al.* (2015) Inter-individual differences in CpG methylation at D4Z4 correlate with clinical variability in FSHD1 and FSHD2. *Hum. Mol. Genet.* **24,** 659–669 CrossRef Medline
28. Sacconi, S., Lemmers, R. J., Balog, J., van der Vliet, P. J., Lahaut, P., van Nieuwenhuizen, M. P., Straasheijm, K. R., Debipersad, R. D., Vos-Versteeg, M., Salviati, L., Casarin, A., Pegoraro, E., Tawil, R., Bakker, E., Tapscott, S. J., *et al.* (2013) The FSHD2 gene SMCHD1 is a modifier of disease severity in families affected by FSHD1. *Am. J. Hum. Genet.* **93,** 744–751 CrossRef Medline
29. Graham, J. M., Jr., and Lee, J. (2006) Bosma arhinia microphthalmia syndrome. *Am. J. Med. Genet. A* **140,** 189–193 Medline
30. Pearl, L. H., Prodromou, C., and Workman, P. (2008) The Hsp90 molecular chaperone: an open and shut case for treatment. *Biochem. J.* **410,** 439–453 CrossRef Medline
31. Prodromou, C. (2012) The "active life" of Hsp90 complexes. *Biochim. Biophys. Acta* **1823,** 614–623 CrossRef Medline
32. Leidenroth, A., Sorte, H. S., Gilfillan, G., Ehrlich, M., Lyle, R., and Hewitt, J. E. (2012) Diagnosis by sequencing: correction of misdiagnosis from FSHD2 to LGMD2A by whole-exome analysis. *Eur. J. Hum Genet.* **20,** 999–1003 CrossRef Medline
33. Achilleos, A., and Trainor, P. A. (2015) Mouse models of rare craniofacial disorders. *Curr. Top. Dev. Biol.* **115,** 413–458 CrossRef Medline
34. Tsutsumi, S., Mollapour, M., Prodromou, C., Lee, C. T., Panaretou, B., Yoshida, S., Mayer, M. P., and Neckers, L. M. (2012) Charged linker sequence modulates eukaryotic heat shock protein 90 (Hsp90) chaperone activity. *Proc. Natl. Acad. Sci. U.S.A.* **109,** 2937–2942 CrossRef Medline
35. Meyer, P., Prodromou, C., Hu, B., Vaughan, C., Roe, S. M., Panaretou, B., Piper, P. W., and Pearl, L. H. (2003) Structural and functional analysis of the middle segment of hsp90: implications for ATP hydrolysis and client protein and cochaperone interactions. *Mol. Cell* **11,** 647–658 CrossRef Medline
36. Retzlaff, M., Stahl, M., Eberl, H. C., Lagleder, S., Beck, J., Kessler, H., and Buchner, J. (2009) Hsp90 is regulated by a switch point in the C-terminal domain. *EMBO Rep.* **10,** 1147–1153 CrossRef Medline
37. Piper, P. W., Millson, S. H., Mollapour, M., Panaretou, B., Siligardi, G., Pearl, L. H., and Prodromou, C. (2003) Sensitivity to Hsp90-targeting drugs can arise with mutation to the Hsp90 chaperone, cochaperones and plasma membrane ATP binding cassette transporters of yeast. *Eur. J. Biochem.* **270,** 4689–4695 CrossRef Medline
38. Prodromou, C., Panaretou, B., Chohan, S., Siligardi, G., O'Brien, R., Ladbury, J. E., Roe, S. M., Piper, P. W., and Pearl, L. H. (2000) The ATPase cycle of Hsp90 drives a molecular "clamp" via transient dimerization of the N-terminal domains. *EMBO J.* **19,** 4383–4392 CrossRef Medline
39. Pearl, L. H., and Prodromou, C. (2000) Structure and in vivo function of Hsp90. *Curr. Opin. Struct. Biol.* **10,** 46–51 CrossRef Medline
40. Nozawa, R. S., Nagao, K., Igami, K. T., Shibata, S., Shirai, N., Nozaki, N., Sado, T., Kimura, H., and Obuse, C. (2013) Human inactive X chromosome is compacted through a PRC2-independent SMCHD1-HBiX1 pathway. *Nat. Struct. Mol. Biol.* **20,** 566–573 CrossRef Medline

41. Babon, J. J., and Murphy, J. M. (2013) *In vitro* JAK kinase activity and inhibition assays. *Methods Mol. Biol.* **967,** 39–55 CrossRef Medline
42. Petoukhov, M. V., Franke, D., Shkumatov, A. V., Tria, G., Kikhney, A. G., Gajda, M., Gorba, C., Mertens, H. D., Konarev, P. V., and Svergun, D. I. (2012) New developments in the ATSAS program package for small-angle scattering data analysis. *J. Appl. Crystallogr.* **45,** 342–350 CrossRef Medline
43. Konarev, P. V., Volkov, V. V., Sokolova, A. V., Koch, M. H. J., and Svergun, D. I. (2003) PRIMUS: a Windows PC-based system for small-angle scattering data analysis. *J. Appl. Crystallogr.* **36,** 1277–1282 CrossRef
44. Kelley, L. A., Mezulis, S., Yates, C. M., Wass, M. N., and Sternberg, M. J. (2015) The Phyre2 web portal for protein modeling, prediction and analysis. *Nat. Protoc.* **10,** 845–858 CrossRef Medline